View Article Online
View Journal

Nanoscale

This article can be cited before page numbers have been issued, to do this please use: J. Chen, K. Bhardwaj and S. Carrara, *Nanoscale*, 2025, DOI: 10.1039/D5NR00104H.

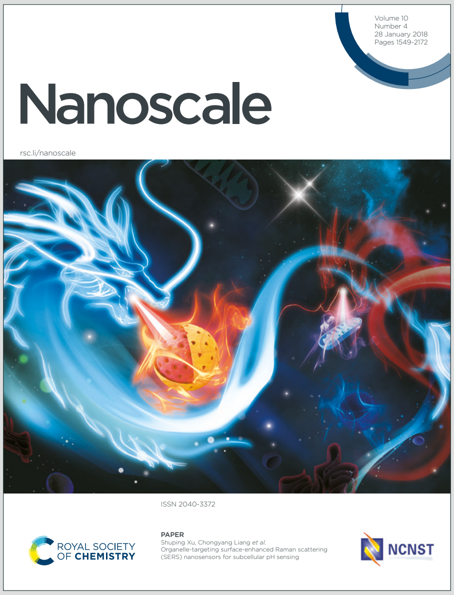

ROYAL SOCIETY
OF CHEMISTRY

rsc.li/nanoscale

View Article Online
DOI: 10.1039/D5NR00104H

ARTICLE

Role of the Oxide in Memristive Quasi-1D Silicon Nanowire†

Junrui Chen,*[a] Kapil Bhardwaj [a‡] and Sandro Carrara [a]

Received 00th January 20xx,
Accepted 00th January 20xx

DOI: 10.1039/x0xx00000x

Memristors are garnering significant attention due to their high similarity to biological neurons and synapses, alongside their unique physical mechanisms. Biosensors exhibiting memristive behaviour have demonstrated substantial efficacy in detecting therapeutic and biological compounds in the past decade. This report investigations on silicon nanowire (SiNW)-based devices incorporating Schottky barriers, which exhibits potential for memristive behaviour. The SiNWs are fabricated between two Nickel (Ni) pads, defined as 1.5 µm in length and 90 nm width, then forming a quasi-one-dimensional (1D) back-to-back Schottky diode structure due to their large aspect ratio. After oxygen plasma treatment of the SiNW, this back-to-back diode structure begins to exhibit memristive behaviour. Our experimental data indicates that this behaviour is induced by superficial oxygen along the SiNW and is influenced by the contacts within the Schottky barrier and intermediate silicon oxide layer. Furthermore, we have developed a mathematical model derived from thermal emission equation of Schottky diodes to accurately characterize and understand this memristive behaviour. Thank to this model, it is possible to accurately fine-tune the design of memristive devices for application to neuromorphic computing and memristive biosensing.

1. Introduction

Since the introduction of the solid-state memristive device based on TiO2 by Strukov and Williams in 2008 [1], the memristive devices have generated significant attention in various domains of application. This high interest can be attributed to their distinctive nonlinear characteristics and exceptional switching properties, including while not limited to low energy consumption, fast switching speed, and high endurance [2-5]. Notably, the memristive devices have firmly established themselves as an potential component in applications such as in memory computing [6], neural networks [7]. Generally speaking, the memristors are categorized into non-volatile and volatile switching behaviours [8]. Non-volatile memristors retain information even after power is turned off, with physical mechanisms rooted to electron spins, ferroelectric polarization, crystalline-amorphous transitions, or interplay between ions and electrons. On the other hand, volatile memristors exhibit spontaneous conductance decay once electrical or optical stimulation stop [8]. Compared to non-volatile devices, volatile memristors possess a unique combination of high similarity to biological neurons and synapses, along with distinctive physical mechanisms [9].

The memristive property was leveraged for the first time in bio-sensing field by our group in 2011, under the term ”memristive biosensor” [10]. An extensive review detailing several ”memristive biosensors” can be found in Carrara [11]. In the context of biosensing, SiNWs are particularly significant due to their substantial aspect ratio and role as a Bio/CMOS interface. SiNW-based biosensors have demonstrated their efficacy in detecting a range of biomolecules, including DNA, proteins, and therapeutic compounds [12-14]. A thorough examination of their applications in carcinoma diagnosis is provided in the comprehensive review by M.-A. Doucey and S. Carrara [15]. SiNW-based memristive biosensors have shown remarkable potential as highly sensitive tools for protein measurement, enabling precise and efficient detection in diverse biological contexts [16,17]. These advancements highlight the far-reaching implications and multifold nature of memristive device research in academia. A critical observation is that upon biofunctionalization, the characteristic memristive pinched current-voltage (I-V) curves are typically lost, leading to the definition of a new parameter known as the ”Voltage gap” [18], and it has been observed the first time in naked nanowires too [19]. This Voltage gap exhibits a proportionality to the concentration of target biomolecules, returning unprecedent limit-of-detection as a biosensing parameter. Collectively, these developments highlight the vast potential and broad applicability of memristive devices in the field of biosensors. In this field, we conclude by throughout our past results that our memristive devices based on SiNWs predominantly exhibits a non-crossing anti-clockwise loop, indicating the volatile resistive switching behaviour. A recent study highlights that the I-V hysteresis exhibited by bio-functionalized nanowires is determined by their inherent memristive characteristics and the induced capacitive effect caused by the charged biomolecules [20]. This insight further emphasizes the potential of SiNW-based memristive biosensors in detecting and analyzing biological compounds with high sensitivity and specificity.

---

[a] *Bio/CMOS Interfaces Lab, Institute of Electrical and Micro Engineering, Engineering Faculty, École Polytechnique Fédérale de Lausanne, Rue de la Maladiere 71b, Neuchatel, 2000, Switzerland*
** Email: junrui.chen @epfl.ch.*

† Supplementary Information available: [details of any supplementary information available should be included here]. See DOI: 10.1039/x0xx00000x

‡ Current affiliation: Thin Film Electronics Lab, Faculty of Information Technology and Communication Sciences, Tampere University, FinlandEXAMPLE

View Article Online
DOI: 10.1039/D5NR00104H

Nevertheless, the mechanism responsible for the origin of this volatile memristive behaviour in quasi-1D structure still eludes the full understanding. The resistive switching effect produced by most of the popular memristive architectures belongs to the formation of a conductive filament (CF) inside a dielectric medium [21-23]. The CF memristive device is typically known for its characteristic "sandwich-like" structure [24], which comprises a thin dielectric layer positioned between the bottom and top electrodes, e.g., in a highly limited volume toward quasi-0 structure. On the other hand, resistive switching has been observed in several kind of 1D and 2D structures made of, while not limited to, silicon [19], gold [25], graphene [26], and organic polymers [27]. These further switching structures are challenging since that do not present the possibility to form the conductive filaments, due to the long-length of the conductive channel. Therefore, 1D memristive device are not simply explained by the CF model.

In addition, the utilization of metal-semiconductor (Schottky) contacts has emerged as a promising alternative for non-filamentary memristive devices, as evidenced by several academic studies [28-34]. Notably, a recent research endeavour led by Zhou et al. [35] introduces a two-dimensional structure based on back-to-back Schottky diodes connected through a planar channel semiconductor. The resulting device exhibits both crossing and non-crossing hysteresis loops for varying voltage sweep, which are associated to volatile and non-volatile switching [36], respectively. The switching mechanism in the reported structure has been attributed to the migration of defects, resulting in redistribution of defect concentration within the device. Consequently, alterations in defect concentration and the Schottky barrier at the contacts, lead to variations in contact resistance as well as in the resistance of the semiconductor layer. Thus, Schottky-diode-modulated memristive devices basically rely on the interplay of various mechanisms, including defects redistribution, charge carrier mobility, Schottky barrier height (SBH), and interface properties. Changes in any of these factors can impact the memristive properties of the device [36].

Interestingly, an effective quasi-1D memristive device has been realized utilizing ZnO nanowire, incorporating Schottky contacts in both terminals [37]. In this device, the induction of a low-resistance state is achieved through the accumulation of vacancies in the barrier enhancement layer, resulting in the formation of local conductive filament channels upon the application of external voltage. Through tuning the set/reset voltage, the ZnO based device presents non-volatile memristive behaviour. Besides tuning of the SBH, the trap-assisted tunneling effect through Schottky barrier at the metal electrode contact has been demonstrated as a pivotal factor in eliciting the both volatile and non-volatile memristive behaviour, particularly in oxide-based device [38].

Enhancing the comprehension of the mechanisms and modelling underlying volatile memristive behaviour is crucial for optimizing the fabrication of memristive biosensors. This is particularly significant when considering the modeling of the capacitive-coupled effect induced by absorbed biomolecules [20,39]. Therefore, this report aims to utilize experimental data to uncover the origins of volatile memristive behaviour and to identify the factors influencing the switching properties in SiNW- based memristors.

The report describes the fabrication of the devices, realized with central SiNWs connected between two Nickel/Nickel silicide (Ni/NiSi) electrodes, which form a back-to-back diode structure connected through a silicon channel. Our findings, both experimental and theoretical, clearly demonstrate that a pure diode structure is unable to explain the measured hysteresis. Robust volatile memristive properties are observed after the device undergoes native oxidization or oxygen plasma treatments. The extent of hysteresis is highly influenced by the SBH and by the characteristics of the oxide intermediate layer.

Model simulations perfectly align with fabricated device and demonstrates no hysteresis for the newly fabricated samples. To explain the influence of the surface oxide layer, an energy-based model is introduced, revealing the origin of the volatile memristive behaviour.

The main scientific contributions of this article are as follows:

1. Developing the robust memristive behaviour in a quasi-1D nanostructure;
2. Experimentally demonstrating that the surface oxide layer is the key factor inducing memristive behaviour, with its properties influenced by Schottky contacts.
3. Promoting an energy-based model that closely aligns with the observed behaviour.

2. Experiment and Methods

2.1. Standard Device formation

A standard fabrication process for SiNWs begins with a top-down, CMOS-compatible technique on a p-type silicon-on-insulator (SOI) substrate with a resistivity range 14-22 Ωcm. The substrate consists of a thin silicon layer and a buried oxide layer, supported by a thicker silicon wafer. To define the pattern for the Ni Pads, a layer of polymethyl methacrylate (PMMA) is precisely patterned using Electron Beam Lithography (EBL). Subsequently, a 50 nm thick layer of Nickel (Ni) is evaporated onto the surface. Then, the excess PMMA layer is removed with acetone, followed by ultrasonic rinsing for 20 minutes. Consequently, the patterned Ni remains on the substrate through the lift-off process. The substrates, now carrying the patterned Ni layer, undergo a annealing step in an inert N_2 ambient under varying annealing conditions. The default annealing condition for standard device is at 400 °C for 20 minutes. This annealing process initiates a reaction between Ni and silicon from the substrate, forming Schottky contacts.

Another EBL process is employed using a 100 nm thick layer of Hydrogen SilsesQuioxane (HSQ) as a negative-tone resist. After exposure and development, the substrate undergoes Deep Reactive Ion Etching (DRIE), also known as the "Bosch Process," to create the silicon nanowires. This process involves alternating etching and passivation steps using SF_6 (etching gas) and C_4F_8 (passivation gas) in a cyclic manner. As a result, stacked silicon nanowires are formed, leaving them suspended between the NiSi contacts. Lastly, the HSQ resist is stripped in a solution comprising 1% HF for 1 minute. The application of 1% HF serves a dual purpose: it strips the HSQ resist and potentially eliminates oxide layers from the SiNW surface. A more comprehensive schematic can be found in Figure S1. The defined SiNWs are captured by Scanning Electron Microscope (SEM).

2.2. Devices Characterization

To characterize the device's behaviour, I-V characteristics are measured by connecting the device to a probe station using tungsten needles under a constant back-gate potential of 0 V. The probe station interfaces with a Sub-Femtoamp 6340 Remote Source Meter, designed by Keithley. This setup efficiently captures and analyses the intricate I-V characteristics, providing comprehensive insights into the memristive behaviour.

2.3. Surface Oxide layer on the Silicon Nanowires

Since the standard device established with HF solution removing the surface oxide layer, the device shows the behaviour like a pure back-to-back diode structure. The I-V curve is obtained using the Source Meter. The voltage window to characterize the memristive behaviour is 4 V, with a default scanning rate of 1 V/s. A series of scanning rates—0.5 V/s, 1 V/s, 2 V/s, and 4 V/s—are employed to analyse the frequency-dependent memristive behaviour. Two parallel strategies are employed to observe the effect of the superficial oxide layer:

Native oxidization: The new device with a pure back-to-back structure is exposed to open air. The I-V curves are monitored over the course of one week.

Oxygen plasma treatment: After immersing in HF solution, the device is treated with oxygen plasma immediately in the "Tepla GiGA- batch". The oxygen gas flow rate is kept at 800 ml/min and plasma power at 600 W for 15 mins to guarantee sufficient oxidization of the silicon nanowire surface.

2.4. Schottky barrier tuning

Varying nickel-to-silicon (Ni:Si) ratios effectively adjusts the SBH at the contacts [40]. Changes in silicidation temperature and duration affect as well. The silicide interface layer gives rise to an increased carrier injection [41], hence a more pronounced melting of Ni and Si atoms leads to a reduction in the SBH [40]. We explored three distinct scenarios for the Schottky contacts formation. Following nickel evaporation, one of the devices undergo silicidation omission, while the remaining two underwent annealing at temperatures of 400 °C for a duration of 20 minutes or 40 minutes, respectively. The color change of the contacts is observed with microscopy, and the interface condition is captured using Back-Scattered electron Detection (BSD).

2.5. Intermediate Oxide layer

Before the definition of the Ni pattern, a thin silicon dioxide layer is sputtered with "Pfeiffer SPIDER 600" onto the top silicon surface, with thicknesses calculated to be 10 nm and 20 nm. After the device is fabricated, an intermediate oxide layer exists between the Ni and Si layers.

3. Results

View Article Online
DOI: 10.1039/D5NR00104H

As captured by the Scanning Electron Microscope (SEM) in Figure 1, the device features two NiSi pads and four stacked SiNWs positioned in between. The SiNWs are approximately 1.45 µm long and 91 nm wide.

3.1. Surface Oxide layer on the Silicon Nanowire

Over the past decade of biosensor research, our group has consistently observed memristive pinched-hysteresis-loop characteristics in the same fabricated devices before biofunctionalization [5,42-44]. It is even more interesting to note that some previous work can be found which demonstrates the Schottky diode-based back-to-back structure exhibits various types of memristive properties, relying on diverse mechanisms [34,36]. In this new paper, we are instead going to elucidate the different effects of the oxide layers as well as the role of the Schottky barrier in the performances of our devices.

3.1.1 Native Oxidization

We have made an interesting observation for our device characteristics over time. Considering the propensity for silicon oxidation in an open environment, Figure 2 presents the evolving electrical characteristics in the I-V plane over time.

Figure 2(a) presents the I-V curve of the brand new fabricated device. It clearly shows a typical electrical property of a back-to-back diode structure. When an external voltage applied on the device, there is always one diode is reverse biased, indicating the maximum current is constrained by the Schottky contacts as saturation current *I0* described by typical thermal emission model in equation 1 [45],

$$I_0 = AA^{**}T^2[\exp(-\frac{q\emptyset_B}{K_B T})] \qquad (1)$$

Where, k_B is the Boltzmann constant, T is the absolute temperature, *A* is the area of the Schottky contact, *A*** is the effective Richardson constant of the semiconductor, ϕ_B is the SBH of a p-type Schottky contact. In the given expression, all parameters, with the exception of the applied voltage, are assumed to remain constant at room temperature. Consequently, during the forward and backward sweep, there is no hysteresis observed, indicating the absence of the memristive behaviour.

With the native oxidation of the silicon nanowires, and then with the oxygen progressively doping the silicon surface, the I-V curve

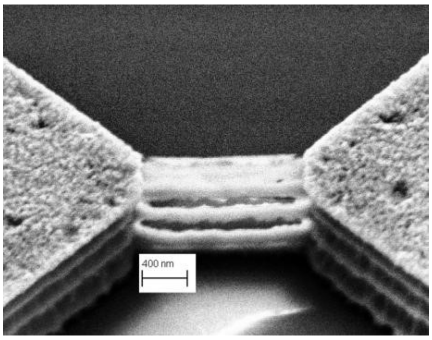

Figure 1: SEM capture of the NiSi-SiNW-NiSi device, tilting with 40°degree.

View Article Online
DOI: 10.1039/D5NR00104H

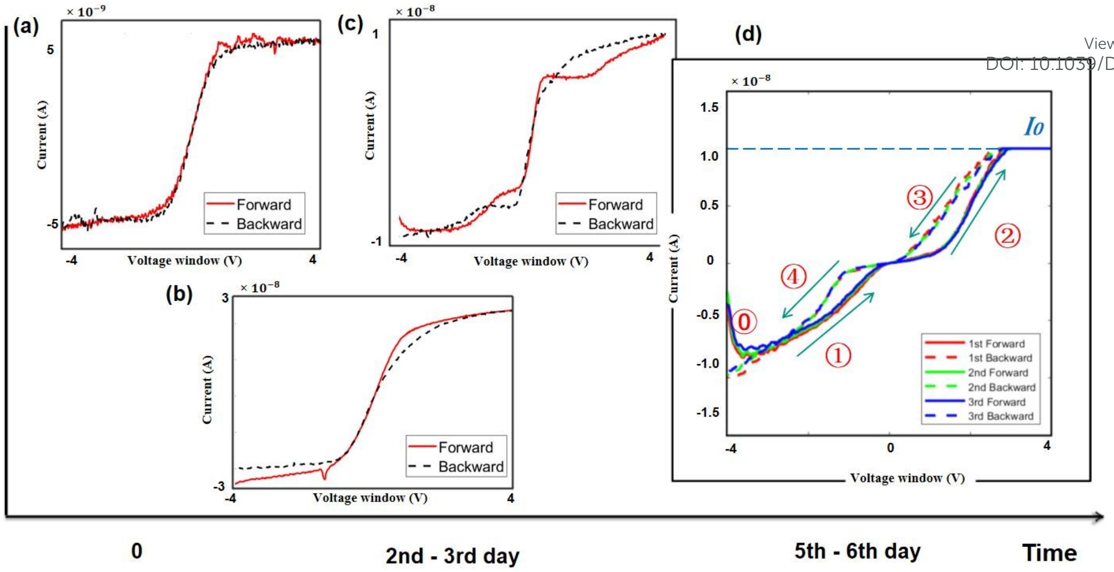

Figure 2: I-V curve of (a) brand new fabricated device, (b-c) the device gradually natural oxidized, showing unpredictable and uncontrollable behaviour . (d) Repeated volatile hysteretic after five days, oxidation process reaches an equilibrium state.

during this period (Figure 2(b&c)) manifests an unpredictable resistance state, exhibiting diverse memristive characteristics. As the oxidation process in open air approaches equilibrium after five days, the I-V curve attains a relatively stable state, revealing pronounced and repeatable analog volatile hysteretic behaviour, as presented in Figure 2(d). An abrupt resistance change occurs when the sweep starts at -4 V in phase ⓪. As the voltage increases, the current eventually stabilizes at the saturation current *I0*, as depicted in Figures 2(a-c), constrained by the Schottky contacts. Phases ① and ③ exhibit a low resistance state as the voltage decreases, while phases ② and ④ exhibit a high resistance state as the voltage increases. From Figure 2(d), we can conclude that the resistive-switching occurs before the current reaches its maximum *I0*.

3.1.2 Oxygen plasma treatment

To avoid the ambiguous hysteretic characteristics as shown in Figure 2 (b&c), the devices are oxidized in a sufficient oxygen plasma atmosphere at 600 W for 15 minutes. On the other hand, Oxygen plasma treatment is also employed to eliminate the organic residuals and activate the silicon surface prior to biofunctionalization [44]. During the oxygen plasma treatment, the SiNWs undergo substantial ions generation within its bulk region due to the absorbed oxygen atoms, resulting in the modification of the physical properties of the SiNWs [46]. Thus, in real-time operation, high-power oxygen plasma treatment can enhance the charge-carrier concentration in the nanowires. Considering the quasi-1D nature of the device due to the extensive length of SiNW, the impact of the oxygen plasma on bulk silicon is considerably more dominant than its effect on the Schottky contacts.

As the devices are newly fabricated, the hysteresis is negligible as presented in semi-logarithmic curve in Figure 3(a). After Oxygen plasma treatment, a very evident hysteresis comes out, as in Figure 3(b). A repeatable volatile memristive behaviour following oxygen plasma treatment within a 4 V voltage window is depicted in Figure 3, referring to the demonstration of the stability of the device. Figure 3(c) shows the same anti-clockwise pinched hysteresis previously obtained with the natural oxidation process illustrated in Figure 2(d). Consistently with the observations in Figure 2(d), an abrupt conductance change is evident when the sweep commences at -4 V.

The reason of this abrupt conductance change is distinctly elucidated by applying a constant external voltage to the device

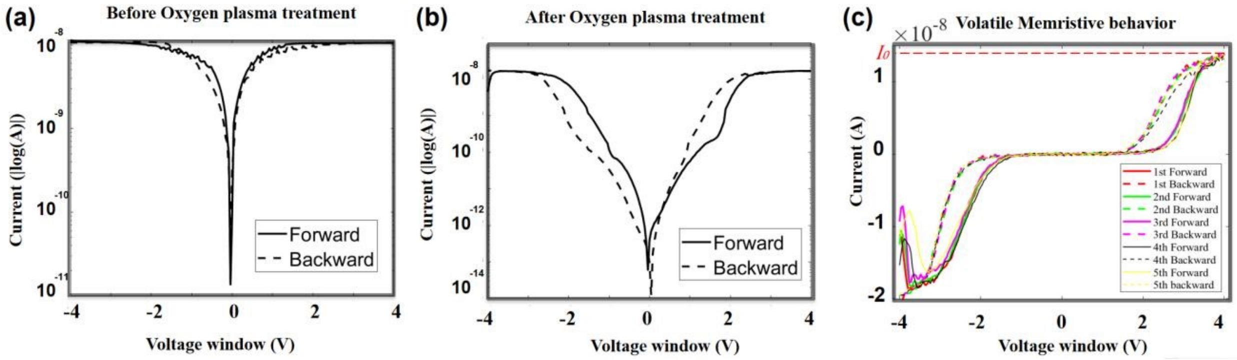

Figure 3: The log(I)-V curve before (a) and after (b) Oxygen plasma treatment. (c) Repeatable and robust volatile memristive behaviour after Oxygen plasma treatment in non-log curve.

View Article Online
DOI: 10.1039/D5NR00104H

before and after the oxygen plasma treatment. The voltage remains at 4 V, meanwhile 200 measures are acquired each 6 ms. The resulting I-V curves are shown in Figure 4. With the device before the plasma treatment, the current remains around 15 nA, consistently with the constrained current observed in Figure 2(a). On the other hand, a clear variation in conductance is observed in the device as measured after the oxygen plasma treatment. The current gradually increases from almost 0 A to approximately 12 nA, indicating a transition from a high-resistance state to a low-resistance state. This conductance change corresponds to the phase labeled ⓪ in Figure 2(d). This data clearly demonstrates that the injection of carriers due to an applied voltage as per the memristive effect is possible only in the presence of the oxygen in the silicon nanowires. Moreover, when the input starts at 1V (Figure 4b), the current remains around 10 pA. Upon increasing the voltage to 4V, the current rises gradually, indicating a transition to the switch-on state. When the voltage returns to 1V, the current decreases accordingly, reverting to the switch-off state, thereby demonstrating volatile behaviour.

As foreseen by the modelling proposed originally also to 0D memristive device [1] the switching behaviour of memristors is expected going down with the sweeping-frequency of the applied voltage going up [47]. Our memristive devices are subject to the same phenomenon as well. The Source Measure Unit is the used to demonstrate this property by supplying sweeps at different scanning rates. As shown in Figure 5, memristive loops are obtained with scanning rates from 4 V/s down to 0.5 V/s. However, it is evident that with the extent of the hysteresis loop becomes more pronounced by decreasing the scanning rate. This observation corresponds to result previously reported in literature that show smaller frequencies leading to more memristive properties.

Intuitively, we see that also by a simply expression in circuitry, $E = VIt$. It easily confirms us that when the scanning rate decreases, which means larger period t, the hysteresis loop moves towards original point in Figure 5, meaning less voltage required correspondingly. This simple energy-related consideration will guide us to the modeling and simulations shown later in Section 4.

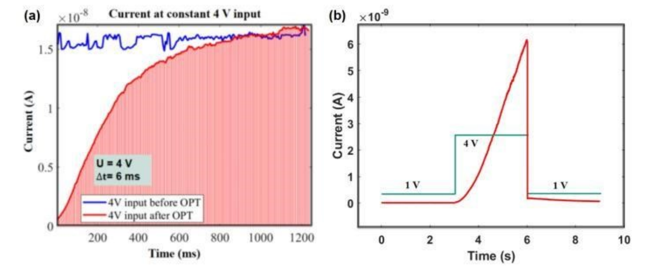

Figure 4: (a) Current measurement at constant 4 V input before and after Oxygen plasma treatment (OPT). (b) Volatility test.

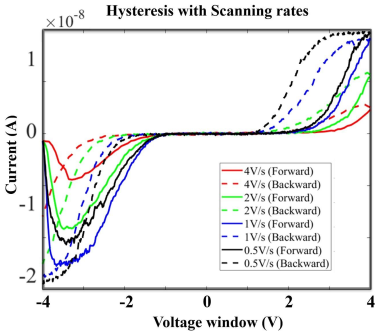

Figure 5: Memristive behaviour with Scanning rates.

3.2. Schottky barrier tuning

The SiNWs-based device also incorporates two Schottky diodes. The impact of Schottky contacts is illustrated in Figure 6, and demonstrates the effect of different annealing conditions on the Ni-Si contacts. The microscopic analysis shown in Figure 6(a) reveals significant changes in the contact surface colour corresponding to different annealing extents. In the absence of annealing, the Ni surface appears rose (Picture (III) in Figure 6(a)). When annealed at 400 ° C for 20 minutes, the surface colour changes to orange (Picture (II) in Figure 6 (a)). With further annealing, the colour further shifts to blue, indicating an increased intermixing of Ni and Si (Picture (I) as directly observed in the SEM images in Figure 6 (a)).

Given the thin Ni layer, BSD is further employed from the top side to observe the atomic distribution at the edge of Ni deposition. Without annealing, the high SBH between Si and Ni results in an unfocused electron beam and a blurred image at 30k × magnification, as shown in the bottom Figure. Energy-dispersive X-ray (EDX) analysis in this case detects only Ni atoms. Annealed devices under conditions of 400 °C for 20 minutes and 400 °C for 40 minutes, as depicted in Figures 6(a).I&II, exhibit the presence of NiSi grains on the surface. Atomic diffusion extends up to 375 nm from the Ni edge. EDX analysis reveals a composition of 5.11% Si by mass and 94.89% Ni. With prolonged annealing for another 20 minutes, the diffusion length increases to 825 nm, and the EDX analysis indicates a Si content of 7.28% and a Ni content of 92.72%.

The measured I-V curves are illustrated in Figure 6(b), exhibiting a shape align to that in Figure 5. The volatile memristive behaviour also displays a comparable trend when altering annealing conditions. As the device undergoes more extensive annealing, the saturation current also varies. The read-out saturation currents I_{0H} is 12.2 nA, I_{0M} is 7.8 nA, and I_{0L} is 2.3 nA under annealing conditions of 400 °C for 40 minutes, 400 °C for 20 minutes, and no annealing, respectively.

When Ni is in direct contact with Si, the SBH is determined by the difference in their work functions and the alignment of their Fermi levels. However, during annealing, Ni reacts with Si to form the compound nickel silicide. This reaction changes the electronic state density and chemical properties at the interface, resulting in a modified SBH. Furthermore, the compound phase has a distinct work function compared to pure Ni, which directly influences the barrier height Concurrently, the experimental data in Figure 6(b) demonstrate that the saturation current increases I_0 with the annealing. Coherently with the equation 1,

$$I_0 \propto \exp(-\phi_B)\,, \tag{2}$$

the saturation current I_0 exhibits an inverse exponential relationship with the SBH (ϕ_B). The observation of annealing aligns with theoretically decreasing SBH. Furthermore, the hysteresis loop width diminishes with higher saturation currents. Combining with the energy-related consideration $E = VIt$, a higher Schottky barrier

View Article Online
DOI: 10.1039/D5NR00104H

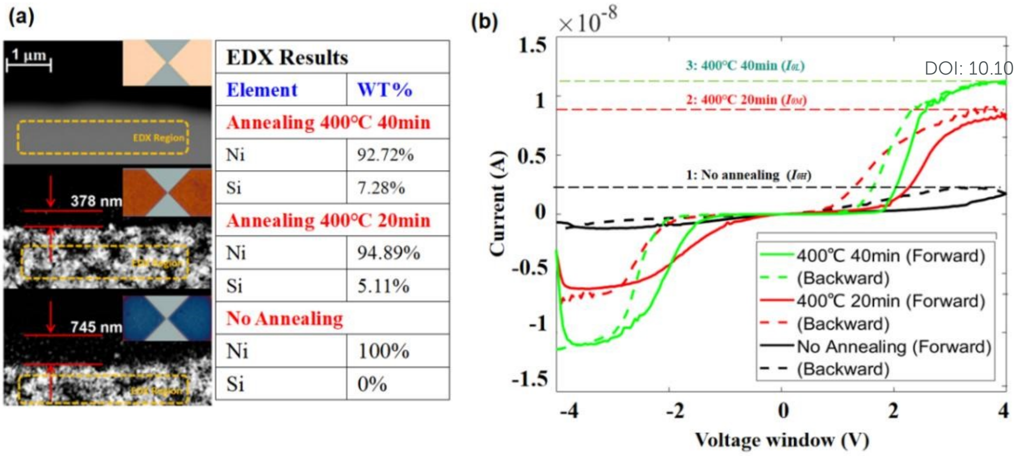

EDX Results	
Element	**WT%**
Annealing 400°C 40min	
Ni	92.72%
Si	7.28%
Annealing 400°C 20min	
Ni	94.89%
Si	5.11%
No Annealing	
Ni	100%
Si	0%

Figure 6: Schottky barrier tuning: (a) The Si-Ni contacts annealing observed in SEM images and (b) the memristive behaviour related to different annealing scenarios

results in a lower saturation current *I0,* and necessitates a higher switching voltage to compensate the required energy for the increased potential (ϕ_B) introduced by annealing treatment.

3.3. Intermediate Oxide layer at the Schottky Contacts

This memristive device features two basic components, the quasi-1D silicon channel and two Schottky-contacts aside. Our previously-described experiments have highlighted the influences of these two device-components on the memristive behaviour. It has been observed that robust volatile memristive behaviour emerges only in the presence of oxygen on the silicon channel. In this section, we further explore instead the role of an intermediate oxide layer between Ni and Si at the Schottky-contact.

In this series of different fabrications, layers with various thicknesses of silicon oxide were sputtered onto the Silicon-on-Insulator chip before the deposition of the Ni, in order to ensure the presence of an oxide layer between the Ni and Si. Three scenarios are here considered: 0 nm, 10 nm, and 20 nm of oxide layer, as schematically sketched in Figure 7(a). Under optical-microscopic examination, the standardized annealing process (400 ℃ for 20 or 40 minutes) results in Schottky contact surface colors of yellow or white, while no annealing results in orange as shown in Figure 7(b). The I-V characteristics of these three different fabrications have been acquired after the Oxygen Plasma Treatment (OPT) of the quasi-1D silicon channel and are presented as well in Figure 7(b). In the absence of an oxide layer, the memristive behaviour, represented by the red curve, resembles that shown in Figure 3(c). The green and black curves represent the cases of 10 nm and 20 nm oxide layers, respectively. The presence of the oxide layer alters the memristive behaviour, notably enlarging the hysteresis loop in the positive voltage region compared to the negative voltage region.

Figure 7(b) shows that, at -4 V, the I-V curve for the 20 nm oxide layer (black curve) starts at a lower current compared to the 10 nm oxide layer (green curve). Interestingly, a thicker oxide layer corresponds to a higher maximum current. At the beginning of the backward sweep, the current continues to increase despite the voltage starts decreasing. This indicates a more complex underlying mechanism compared to that depicted in Figure 3. The switching mechanism involving the intermediate oxide layer has been

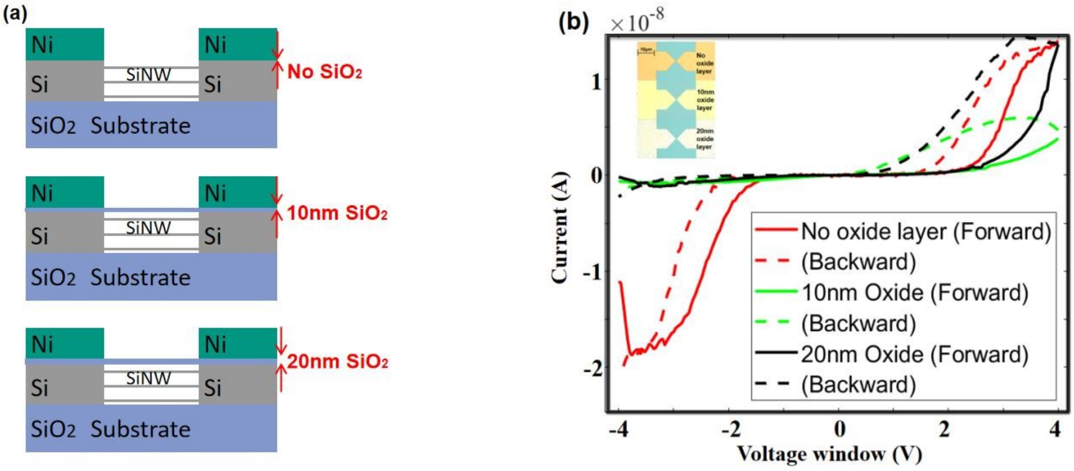

Figure 7: (a) Schematic of the intermediate oxide layer. (b) Memristive behaviour with different thickness of different intermediate Oxide layer.

View Article Online
DOI: 10.1039/D5NR00104H

extensively discussed by Mehonic et al. in prior studies [48]. In the forward sweep, initially at -4 V, the current is impeded by the insulating silicon oxide layer, resulting in significantly lower currents with respect the current we measure at -3.9 nA. Then, the formation of conductive filaments within the oxide layer, driven by oxygen vacancies and ions, begins under the negative applied voltage [49]. As the voltage continues to be applied, a substantial number of conductive bridges are formed, then leading to a scenario where the current continues to increase even as the applied voltage decreases during the backward sweep. The thicker oxide layer provides more oxygen vacancies, then more conductivity at the nanoampere scale.

4. Modelling and simulation

In order to deeply understand the experimental findings reported so far from a more comprehensive theoretical point of view, we have also developed a quite simple modelling of our device, and obtained accordingly simulation outputs to demonstrate the main features of the device properties. The present session of the paper is dedicated to this theoretical aspect of our work.

4.1. The back-to-back diodes structure

As depicted in Figure 8(b), the back-to-back diodes structure incorporates a conducting channel, and two Schottky diodes, denoted as Dl and Dr , subjected to a forward voltage sweep followed by a reverse sweep, as shown in Figure 8(a). The voltage applied across the device can be distributed as:

$$\mathrm{V_{AB}} = \mathrm{V_{Dl}} + \mathrm{V_{Si}} + \mathrm{V_{Dr}} \,. \tag{3}$$

In such a scheme, there is always be at least one diode operating in a reverse-biased configuration. For instance, if the current flows from node

A to B, diode Dl is forward biased while Dr is reverse biased. This is expressed as:

$$\mathrm{R_{Dr}} >> \mathrm{R_{Dl}},\ \mathrm{R_{Dr}} >> \mathrm{R_{Si}} \,. \tag{4}$$

which leads to,

$$\mathrm{V_{AB}} \approx \mathrm{V_{Dr}}. \tag{5}$$

Figure 8(c) presents a static I-V curve of a single diode. It comprises three distinct regions: the breakdown region, reverse saturation region, and thermionic emission region. The thermionic emission and the saturation current of the diode are both involved in the Shockley diode equation [50-51]:

$$\mathrm{I} = \mathrm{I_0}[\exp(\frac{\mathrm{V}}{\mathrm{V_t}}) - 1] \tag{6}$$

In here, the saturation current *I₀* is obtained by the in equation 1, and, V represents the voltage applied across the diode. $V_t = \eta k B\, T/q$ is instead the thermal voltage, where η is the ideal factor usually chosen as 1 [50,52] in a regular Schottky diode. Equation 5 suggests that the device operation is mainly governed by the reverse-biased diode. Thus, the area of interest labeled with red frame in Figure 8(c) is only the reverse biased region before breaking down. This region is defined as:

$$|\mathrm{V_{AB}}| < |\mathrm{V_{bd}}| \,. \tag{7}$$

Thus, the current going through the device in one direction is

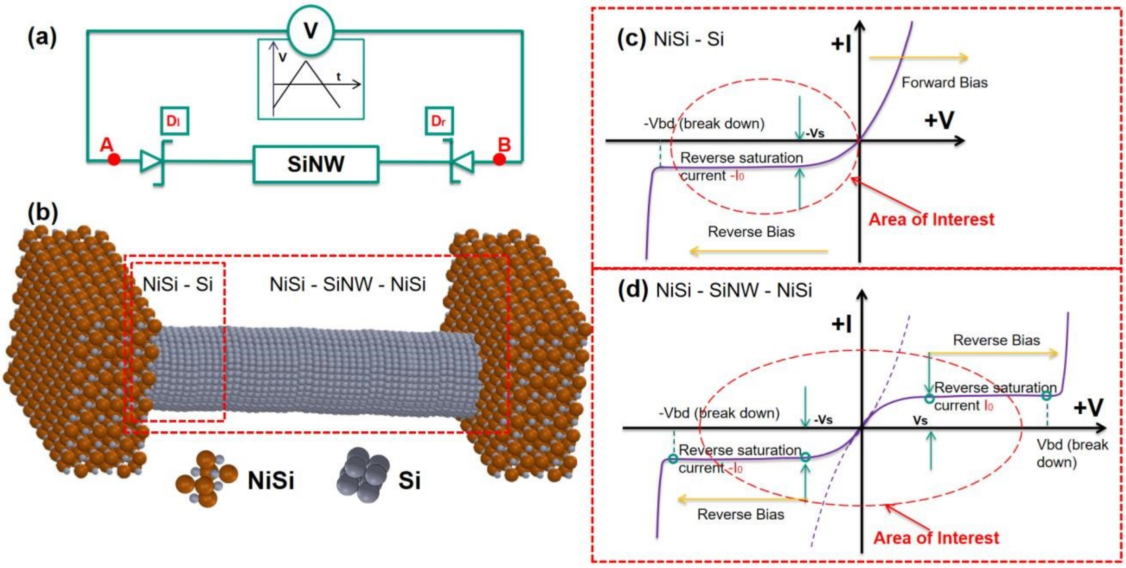

Figure 8: (a) Scheme of driving back-to-back Schottky diodes structure with a triangular waveform-signal. (b) Schematic of back-to-back Schottky diodes structure formed across SiNW with triangular signal. (c) I-V characteristics of a single diode. (d) I-V characteristics within a single voltage sweep through the back-to-back Schottky diodes structure.

written as:

$$I_{AB} = I_{Dr} = I_0[\exp(\frac{V_{AB}}{V_t} - 1)]. \tag{8}$$

As discussed above, the electrical behaviour of the Schottky-barrier modulated SiNW can be described by the operation of a reverse-biased diode in both negative/positive cycles of the input signal. The Figure 8(d) shows an I-V characteristics model curve representing the integration of two back-to-back diodes. In the area of $|V_{AB}| < |V_S|$, the dashed line represents the dominance of carriers generated by the thermionic emission (gradual increase in current), while the solid current denotes the saturation due to the energy barrier (constant current). As a result, the conduction characteristic of the back-to-back diodes structure can be split into five regions separated by the break down voltages and saturation voltages marked with green circles, where the area of interested is marked with red frame as defined by equation (7). Consequently, the current going through the device under voltage sweep can be described in equations 9 within the "Area of Interest" :

$$I_{AB} = \tag{9}$$

$$\begin{cases} -I_0, & -V_{bd} < V_{AB<} - V_s \\ I_0[\exp(\frac{qV_{AB}}{K_BT}) - 1], & -V_s < V_{AB} < 0 \\ -I_0[\exp(\frac{qV_{AB}}{K_BT}) - 1], & 0 < V_{AB<} V_s \\ I_0, & V_s < V_{AB<} V_{bd} \end{cases}$$

From equations (9), we have conducted in MATLAB mathematical simulations using an array as a window of input voltages to obtain an array of computed current values. The accordingly-obtained normalized I-V characteristics are depicted in Figure 9. As well, a brandy-new fabricated device, as seen in Section 2, manifests nearly superimposed curves during both forward and backward sweeps, as per the measured result in Figure 2(a), which corroborates the model.

4.2. Volatile memristive behaviour

The volatile memristive behaviour is assumed to be energy-related as described in section 3.1 and 3.2. In equation 1, the $(q\emptyset_B)$ part is the energy term determined by the SBH $(\emptyset_B)$. However, SBH is not constant in the actual diode. There is Schottky barrier lowering, also names as image force lowering, $q(\emptyset_B - \Delta\emptyset_B)$ [53-54], which is governed by the drain and source bias, along with the energy consumption to overcome the energetic band separation from the conduction band, concluded in equation 10 [55]:

$$\Delta\emptyset_B \propto (\emptyset_B + V_R - \emptyset_p)^{\frac{1}{4}} \tag{10}$$

where $\emptyset_P$ is the potential difference between valance band and the Fermi level of the p-type semiconductor, considered as a constant. The detailed introduction of the image force lowering effect can be found in [55]. However, a precise relationship is still a subject of debate. The experimental plots delineated in the report [56] provide empirical evidence supporting that the image force lowering is proportional to the square root of the electric field across the semiconductor depletion region, and the forward characteristic is less affected than the reverse characteristic. The prevailing consensus is that the reduction in barrier height exhibits a positive correlation with the applied voltage [57]. Thus, an energy-related term is used to compensate the impact from the input energy E_{in} on I-V relationship by equation (6), and presented in equation (11):

$$I_{AB} = I_0[\exp(\frac{V_{AB}}{V_t}) - 1]f(E_{in}). \tag{11}$$

$$f(E_{in}) = \exp(\frac{E_{in}}{K_BT}) = \exp(\frac{f(\int V(t)I(V)dt)}{K_BT}) \tag{12}$$

For an instantaneous moment, the instant input energy δEin is defined as:

$$\delta E_{in} = K_S \ln(VI\delta t) + 1. \tag{13}$$

where the K_S is the coefficients influenced by SBH. For an actual sweep, integral is converted into series, by:

$$E_{in} = \sum \delta E_{in}^n. \tag{14}$$

Solving with an iterative way, the adjusted I-V relationship can be then described as:

$$I_{AB}^{n+1} = I_0[\exp(\frac{V_{AB}^n}{V_t}) - 1]\exp(\frac{K_S \ln(V_{AB}^n I_{AB}^n \delta t) + 1}{K_BT}) \tag{15}$$

Finally, the mathematical model to simulate the memristive behaviour of back-to-back diodes structure is written as equations (16), combined with equation (15).

$$I_{AB} = \tag{16}$$

$$= \begin{cases} -I_0, & -V_{bd} < V_{AB<} - V_s \\ I_0[\exp(\frac{qV_{AB}}{K_BT}) - 1]f(E_{in}), & -V_s < V_{AB} < 0 \\ -I_0[\exp(\frac{qV_{AB}}{K_BT}) - 1]f(E_{in}), & 0 < V_{AB<} V_s \\ I_0, & V_s < V_{AB<} V_{bd} \end{cases}$$

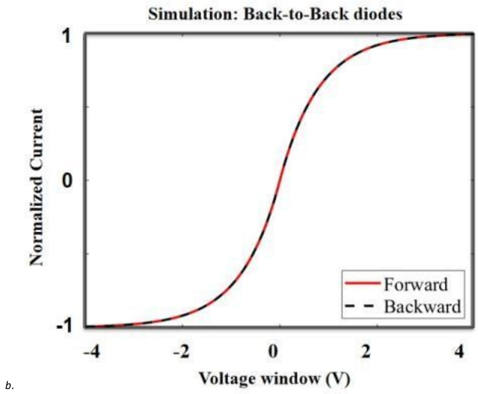

Figure 9: The simulated current of a pure back-to-back diodes.

View Article Online
DOI: 10.1039/D5NR00104H

View Article Online
DOI: 10.1039/D5NR00104H

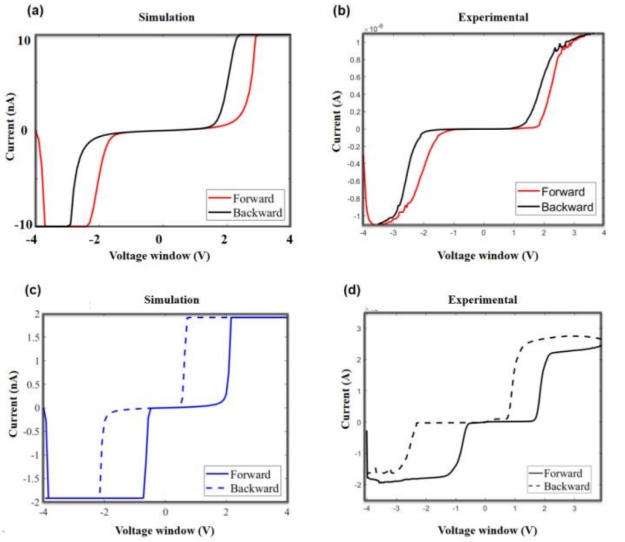

Figure 10: The comparison of simulated and experimental data. (a) The simulation results with higher saturation current. (b) A representative measured I/V curve with annealed device, showing higher saturation current and small hysteresis. (c) The simulation results with lower saturation current. (d) A representative measured I/V curve of the device without annealing, showing lower saturation current and greater hysteresis.

By adjusting the parameters, the simulated results closely align with the experimental data, as demonstrated in Figure 10. In Figure 10(a), the simulated memristive behaviour is shown with I_0 to 10 nA. The actual I-V curve, presented in Figure 10(b), corresponds to a representative sample of an annealed device with a saturation current of approximately 12 nA. When I_0 is reduced to 2 nA in Figure 10(c), the memristive behaviour exhibits a more pronounced hysteresis. This aligns with the behaviour of an unannealed device, which has a higher SBH. Correspondingly, in Figure 10(d), an unannealed device with a SBH shows a saturation current of around 2 nA, matching the simulated behaviour. This comparison confirms that the simulation results accurately replicate the actual device characteristics under different conditions, demonstrating a strong alignment between the model and experimental observations. For more detailed simulation, see Supplementary Material, in Figure S2&S3 for the frequency-dependent behaviour and Schottky barrier influence, respectively.

5. Discussion

The proposed model is simplified, focusing primarily on the energy-related term under ideal conditions and neglecting factors such as interface defects and parasitic effects. Despite these simplifications, the comparison between simulated and experimental data shows no significant discrepancies, as the simulation successfully incorporates the key features of volatile memristive behaviour.

To better understand this type of volatile memristive behaviour, an 8 V voltage window is used to highlight the key features, as shown in Figure 11:

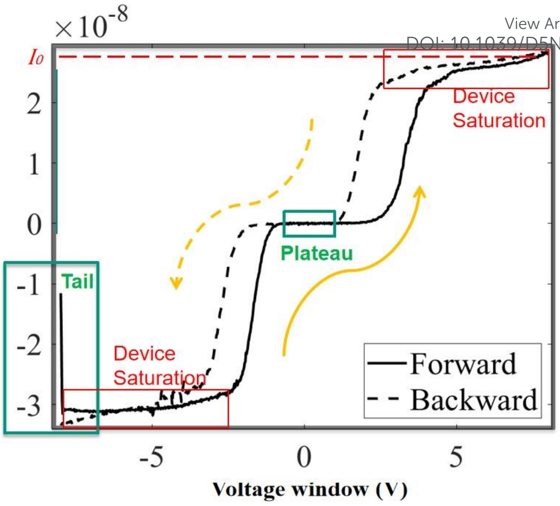

Figure 11: The Key features of complete non-crossing anti-clockwise hysteresis loop with input voltage window (8V).

1. **Tail effect:** When the sweep initials, a "tail" appears, representing a sudden conductance change, consistent with the behaviour shown in Figure 4.
2. **Central Plateau:** In the central region, the current remains nearly zero, forming a plateau. This can be explained by the energy-compensation assumption, where the device requires sufficient energy input to overcome the high-resistive state.
3. **Saturation Current:** The current saturates at a specific value (I_0) due to the rectification effect of the Schottky contacts. Even at higher input voltages, the current remains almost constant around I_0.
4. **Non-Crossing, Anti-Clockwise Hysteresis:** The I-V curve exhibits non-crossing, anti-clockwise hysteresis.

The simulation by Equation 16 successfully reproduces these four key features, aligning well with the experimental observations.

Notably, for this single device in Figure 11, the saturation current in the negative region is higher than in the positive region, attributed to fabrication errors at the Schottky contacts. Consequently, the hysteresis in the negative region is noticeably thinner than in the positive region. This behaviour is consistent with the results shown in Figure 6, where a higher SBH leads to more pronounced memristive hysteresis.

This observation underscores that, although unpredictable errors may occur during actual fabrication, the overall results remain highly consistent with the fundamental principles derived in this paper. This demonstrates that, even under complex fabrication conditions, the proposed model and principles are highly applicable and reliable, offering both theoretical guidance and experimental validation for the further optimization and design of similar devices.

6. Conclusion

This report investigates role of the oxide in Quasi-1D memristive devices made with silicon nanowires, typically proposed over the last decade of published experiments for memristive biosensors. These kinds of memristive devices comprise two Schottky contacts and stacks of SiNWs. Thanks to the oxidation of SiNWs, the devices

View Article Online
DOI: 10.1039/D5NR00104H

demonstrate robust volatile memristive behaviour along with the expected frequency-dependent properties. Additionally, we have demonstrated that tuning the SBH of the metal contacts significantly affects the device ' s characteristics. The higher SBH results in greater extent of hysteresis. Furthermore, the influence of the intermediate oxide layer placed in between the Schottky contacts has been also investigated and discussed. This oxide layer acts to amplifies the hysteresis. Finally, a model based on thermal emission has been proposed grounded to the energy-related assumptions. This model has actually shown a very well alignment with the observed experimental measurements.

The several evidences investigated in this report also play as key role in designing and optimizing memristive biosensors. Therefore, this research ultimately paves the way for a better development of new categories of volatile memristive devices and guides further more precisely designs in memristive biosensing.

Author contributions

J.Chen: Writing – review & editing, Writing – original draft, Methodology, Experiments, Simulations, Investigations, Formal analysis.
S. Carrara: Writing – review & editing, Conceptualization Supervision, Validation, Project administration, Funding acquisition, Resources.
K. Bhardwaj: Writing – review & editing, Methodology, Simulations.

Conflicts of interest

There are no conflicts to declare.

Data availability

Data for this article are available at [Github] at [https://github.com/JunruiChen666/Memristive-behavior].

Acknowledgements

The authors acknowledge the financial support by the Swiss National Science Foundation (SNSF) with the project titled ”In-memory sensing”. The innosuisse project with acronym ¨ Onco-PoK2¨ is acknowledged as well for co-funding of this research.The authors would like to acknowledge all the CMi staff of EPFL for their valuable technical suggestions throughout the fabrication process as well as to Ata Golparval and Gian Luca Barbruni of the BCI Lab in EPFL for their appreciated advice.

Notes and references

1 D. B. Strukov, G. S. Snider, D. R. Stewart, R. S. Williams, nature 453 (2008) 80–83.
2 X.-D. Huang, Y. Li, H.-Y. Li, K.-H. Xue, X. Wang, X.-S. Miao, IEEE Electron Device Letters 41 (2020) 549–552.
3 H. Duan, S. Cheng, L. Qin, X. Zhang, B. Xie, Y. Zhang, W. Jie, The Journal of Physical Chemistry Letters 13 (2022) 7130–7138.
4 S. Pal, S. Bose, A. Islaml, Microsystem Technologies (2019) 1–15.
5 F. Puppo, A. Dave, M.-A. Doucey, D. Sacchetto, C. Baj-Rossi, Y. Leblebici, G. De Micheli, S. Carrara, IEEE Transactions on NanoBioscience 13 (2014) 19–30.
6 D. Ielmini, H.-S. P. Wong, Nature electronics 1 (2018) 333–343.
7 C. Yakopcic, M. T. Taha, in: 2018 Interna- tional Joint Conference on Neural Networks (IJCNN), IEEE, 2018, pp. 1–7.
8 G. Zhou, Z. Wang, B. Sun, F. Zhou, L. Sun, H. Zhao, X. Hu, X. Peng, J. Yan, H. Wang, et al., Advanced Electronic Materials 8 (2022) 2101127.
9 R. Wang, J.-Q. Yang, J.-Y. Mao, Z.-P. Wang, S. Wu, M. Zhou, T. Chen, Y. Zhou, S.-T. Han, Advanced Intelligent Systems 2 (2020) 2000055.
10 D. Sacchetto, M.-A. Doucey, G. De Micheli, Y. Leblebici, S. Carrara, Bio- NanoScience 1 (2011) 1–3.
11 S. Carrara, , IEEE Sensors Journal 21 (2020) 12370–12378.
12 J.-i. Hahm, C. M. Lieber, Nano letters 4 (2004) 51–54.
13 G. Zheng, F. Patolsky, Y. Cui, W. U. Wang, C. M. Lieber, Nature biotechnology 23 (2005) 1294–1301.
14 I. Tzouvadaki, N. Aliakbarinodehi, G. De Micheli, S. Carrara, Nanoscale 9 (2017) 9676–9684.
15 M.-A. Doucey, S. Carrara, Trends in biotechnology 37 (2019) 86–99.
16 I. Tzouvadaki, C. Parrozzani, A. Gallotta, G. De Micheli, S. Carrara, BioNanoScience 5 (2015) 189–195.
17 I. Tzouvadaki, G. De Micheli, S. Carrara, Applications of Emerging Memory Technology: Beyond Storage (2020) 133–157.
18 Carrara, S., Sacchetto, D., Doucey, M. A., Baj-Rossi, C., De Micheli, G., & Leblebici, Y. (2012). Sensors and Actuators B: Chemical, 171, 449-457.
19 D. Sacchetto, M. H. Ben-Jamaa, S. Carrara, G. De Micheli, Y. Leblebici, in: Proceedings of 2010 IEEE International Symposium on Circuits and Systems, IEEE, 2010, pp. 9–12.
20 K. Bhardwaj, A. Golparvar, J. Chen, G. L. Barbruni, S. Carrara, IEEE Sensors Letters (2023).
21 J. Woo, D. Lee, Y. Koo, H. Hwang, Microelectronic Engineering 182 (2017) 42–45.
22 X. Zhang, S. Liu, X. Zhao, F. Wu, Q. Wu, W. Wang, R. Cao, Y. Fang, H. Lv, S. Long, et al., IEEE Electron Device Letters 38 (2017) 1208–1211.
23 M. Congiu, M. H. Boratto, C. F. Graeff, in zn: Cds thin films, ChemistrySelect 3 (2018) 9794–9802.
24 R. S. Williams, IEEE spectrum 45 (2008) 28–35.
25 Johnson, S. L., Sundararajan, A., Hunley, D. P., & Strachan, D. R. (2010). Nanotechnology, 21(12), 125204.
26 S. Porro, E. Accornero, C. F. Pirri, C. Ricciardi, Carbon 85 (2015) 383–396.
27 T. Berzina, A. Smerieri, M. Bernab`o, A. Pucci, G. Ruggeri, V. Erokhin, M. P. Fontana, Journal of Applied Physics 105 (2009).
28 M. U. Khan, G. Hassan, M. A. Raza, J. Bae, N. P. Kobayashi, Journal of Materials Science: Materials in Electronics 30 (2019) 4607–4617.
29 N. Casa Branca, J. Deuermeier, J. Martins, E. Carlos, M. Pereira, R. Martins, E. Fortunato, A. Kiazadeh, Advanced Electronic Materials 6 (2020) 1900958.
30 Q. Wu, C. Lu, H. Wang, J. Cao, G. Yang, J. Wang, Y. Gong, X. Shi, X. Chuai, N. Lu, et al., IEEE Electron Device Letters 40 (2018) 24–27.
31 Y.-S. Fan, P.-T. Liu, IEEE Transactions on Electron Devices 61 (2014) 1071–1076.
32 S. Rehman, H. Kim, M. F. Khan, J.-H. Hur, J. Eom, D.-k. Kim, Journal of Alloys and Compounds 855 (2021) 157310.
33 G. Milano, M. Luebben, Z. Ma, R. Dunin-Borkowski, L. Boarino, C. F. Pirri, R. Waser, C. Ricciardi, I. Valov, Nature communications 9 (2018) 5151.
34 L. He, Z.-M. Liao, H.-C. Wu, X.-X. Tian, D.-S. Xu, G. L. Cross, G. S. Duesberg, I. Shvets, D.-P. Yu, Nano letters 11 (2011) 4601–4606.

View Article Online
DOI: 10.1039/D5NR00104H

35 H. Zhou, V. Sorkin, S. Chen, Z. Yu, K.-W. Ang, Y.-W. Zhang, Advanced Electronic Materials (2023) 2201252.

36 Y. V. Pershin, M. Di Ventra, Advances in Physics 60 (2011) 145–227.

37 X. Wu, N. Cui, Q. Zhang, X. Xiong, T. Zhu, Q. Xu, Zno Journal of Electronic Materials 51 (2022) 7190–7197.

38 C. Funck, S. Menzel, ACS Applied electronic materials 3 (2021) 3674–3692.

39 B. Sun, Y. Chen, M. Xiao, G. Zhou, S. Ranjan, W. Hou, X. Zhu, Y. Zhao, S. A. Redfern, Y. N. Zhou, Nano letters 19 (2019) 6461–6465.

40 J. Yuan, G. Z. Pan, Y.-L. Chao, J. C. Woo, MRS Online Proceedings Library 829 (2004) 332–337.

41 S. Nagarajan, T. Mikolajick, J. Trommer, Solid-State Electronics 208 (2023) 108739.

42 F. Puppo, M. Di Ventra, G. De Micheli, S. Carrara, Surface Science 624 (2014) 76–79.

43 F. Puppo, M.-A. Doucey, M. Di Ventra, G. De Micheli, S. Carrara, in: 2014 IEEE international sym- posium on circuits and systems (ISCAS), IEEE, 2014, pp. 2257–2260.

44 I. Tzouvadaki, A. Tuoheti, G. De Micheli, D. Demarchi, S. Carrara, in: 2018 IEEE International Symposium on Circuits and Systems (ISCAS), IEEE, 2018, pp. 1–5.

45 R. Enderlein, N. J. Horing, World Scientific, 1997.

46 J. Koo, S. Kim, Solid state sciences 11 (2009) 1870–1874.

47 L. Chua, IEEE Transactions on circuit theory 18 (1971) 507–519.

48 A. Mehonic, A. L. Shluger, D. Gao, I. Valov, E. Miranda, D. Ielmini, A. Bricalli, E. Ambrosi, C. Li, J. J. Yang, et al., Advanced materials 30 (2018) 1801187.

49 A. Mehonic, M. S. Munde, W. Ng, M. Buckwell, L. Montesi, M. Bosman, A. Shluger, A. Kenyon, Microelectronic Engineering 178 (2017) 98–103.

50 W. Shockley, Bell system technical journal 28 (1949) 435–489.

51 C. P. Y. Wong, C. Troadec, A. T. Wee, K. E. J. Goh, Physical Review Applied 14 (2020) 054027.

52 G. Wetzelaer, M. Kuik, M. Lenes, P. Blom, Applied physics letters 99 (2011).

53 Y. Vaknin, R. Dagan, Y. Rosenwaks, Nanomaterials 10 (2020) 2346.

54 F. Puppo, F. L. Traversa, M. Di Ventra, G. De Micheli, S. Carrara, Nanotechnology 27 (2016) 345503.

55 K. K. N. S.M.Sze, John wiley & sons, 2006. doi:DOI:10.1002/0470068329.

56 S. Sze, C. Crowell, D. Kahng, Journal of Applied Physics 35 (1964) 2534–2536.

57 J. Andrews, Journal of Vacuum Science and Technology 11 (1974) 972–984.

View Article Online
DOI: 10.1039/D5NR00104H

Title: Role of the Oxide in Memristive Quasi-1D Silicon Nanowire

Authors' Names: Junrui Chen[a]*, Kapil Bhardwaj[1] and Sandro Carrara[1]
[1]Bio/CMOS Interfaces Laboratory (BCI), École Polytechnique Fédérale de Lausanne, 2000 Neuchâtel, Switzerland

Data availability

Data for this article are available at [Github] at:

[https://github.com/JunruiChen666/Memristive-behavior].